



Estimation of surface impedance at oblique incidence based on sparse array processing

Richard, Antoine Philippe André; Fernandez Grande, Efren; Brunskog, Jonas; Jeong, Cheol-Ho

Published in:
Journal of the Acoustical Society of America

Link to article, DOI:
[10.1121/1.4983756](https://doi.org/10.1121/1.4983756)

Publication date:
2017

Document Version
Publisher's PDF, also known as Version of record

[Link back to DTU Orbit](#)

Citation (APA):
Richard, A. P. A., Fernandez Grande, E., Brunskog, J., & Jeong, C-H. (2017). Estimation of surface impedance at oblique incidence based on sparse array processing. *Journal of the Acoustical Society of America*, 141(6), 4115–4125. <https://doi.org/10.1121/1.4983756>

General rights

Copyright and moral rights for the publications made accessible in the public portal are retained by the authors and/or other copyright owners and it is a condition of accessing publications that users recognise and abide by the legal requirements associated with these rights.

- Users may download and print one copy of any publication from the public portal for the purpose of private study or research.
- You may not further distribute the material or use it for any profit-making activity or commercial gain
- You may freely distribute the URL identifying the publication in the public portal

If you believe that this document breaches copyright please contact us providing details, and we will remove access to the work immediately and investigate your claim.

Estimation of surface impedance at oblique incidence based on sparse array processing

Antoine Richard, , Efren Fernandez-Grande, , Jonas Brunskog, and , and Cheol-Ho Jeong

Citation: [The Journal of the Acoustical Society of America](#) **141**, 4115 (2017); doi: 10.1121/1.4983756

View online: <http://dx.doi.org/10.1121/1.4983756>

View Table of Contents: <http://asa.scitation.org/toc/jas/141/6>

Published by the [Acoustical Society of America](#)

Articles you may be interested in

[Acoustic levitation of an object larger than the acoustic wavelength](#)

The Journal of the Acoustical Society of America **141**, 4148 (2017); 10.1121/1.4984286

[A Marchenko equation for acoustic inverse source problems](#)

The Journal of the Acoustical Society of America **141**, 4332 (2017); 10.1121/1.4984272

[Sound-field measurement with moving microphones](#)

The Journal of the Acoustical Society of America **141**, 3220 (2017); 10.1121/1.4983093

[Finite Element and Boundary Methods in Structural Acoustics and Vibration](#)

The Journal of the Acoustical Society of America **141**, 4300 (2017); 10.1121/1.4984771

[Non-negative intensity for coupled fluid–structure interaction problems using the fast multipole method](#)

The Journal of the Acoustical Society of America **141**, 4278 (2017); 10.1121/1.4983686

[Three-dimensional-printed membrane-type acoustic metamaterial for low frequency sound attenuation](#)

The Journal of the Acoustical Society of America **141**, EL538 (2017); 10.1121/1.4984623

Estimation of surface impedance at oblique incidence based on sparse array processing

Antoine Richard,^{a)} Efren Fernandez-Grande, Jonas Brunskog, and Cheol-Ho Jeong
*Acoustic Technology, Department of Electrical Engineering, Technical University of Denmark (DTU),
 Building 352, Ørstedss Plads, DK-2800 Kongens Lyngby, Denmark*

(Received 18 November 2016; revised 13 April 2017; accepted 7 May 2017; published online 5 June 2017)

A method is proposed to estimate the surface impedance of a large absorptive panel from free-field measurements with a spherical microphone array. The method relies on the reconstruction of the pressure and the particle velocity on the studied surface using an equivalent source method based on spherical array measurements. The sound field measured by the array is mainly composed of an incident and a reflected wave, so it can be represented as a spatially sparse problem. This makes it possible to use compressive sensing in order to enhance the resolution and the quality of the estimation. The results indicate an accurate reconstruction for angles of incidence between 0° and 60°, and between approximately 200 and 4000 Hz. Additionally, experimental challenges are discussed, such as the sample's finiteness at low frequencies and the estimation of the background noise.

© 2017 Acoustical Society of America. [<http://dx.doi.org/10.1121/1.4983756>]

[MV]

Pages: 4115–4125

I. INTRODUCTION

The sound absorption properties of materials, which are typically characterized by the surface impedance Z_s or the absorption coefficient α , are an indispensable input to acoustic simulations and predictions, e.g., in room acoustics, outdoor sound propagation, or the acoustics of vehicle cabins. The two existing standardized measurement methods, the impedance tube method¹ and the reverberation chamber method,² yield limited information, especially in terms of angle dependence. The absorption coefficient is determined at normal incidence with the impedance tube method and at random incidence with the reverberation chamber method. However, information on the phase and angle dependence of absorption is needed in various applications, such as phased room acoustic simulations.³ Another example is the use of the absorption coefficient at 45° incidence in order to approximate *in situ* the random incidence value.⁴ The constraints imposed by laboratory measurements in terms of equipment or sample size have led to the development of various *in situ* measurement methods, as summarized in Ref. 5. Some techniques are based on characterizing the sound field above the sample in order to infer the impedance on the surface, by measuring the pressure at two close points⁶ or the pressure and the particle velocity at the same point.⁷ Alternatively, the absorption coefficient can be derived from the comparison of the incident and the reflected fields. The separation of these two components can be done temporally⁸ or spatially.^{9,10} Various approaches have been proposed to achieve this spatial separation, such as the use of a spatial Fourier transform,⁹ a directional microphone array,¹⁰ or the study of the directions of arrival from a spherical array.¹¹

This paper presents an impedance estimation method based on array measurements and sound field reconstruction.^{12,13} We

consider a sample on which an incident wave impinges at a given oblique angle. The sound field is measured with a spherical microphone array. The array is a rigid sphere, which is omnidirectional, and its scattering effect on the sound field can be compensated for.^{14–17} The measured sound field is expressed as a sum of elementary waves, following an equivalent source method based on spherical array measurements (S-ESM).¹⁸ This wave decomposition is used to reconstruct the pressure and the normal particle velocity on the surface of the absorber. The surface impedance is then derived from these two reconstructed quantities. Furthermore, the sound field is mainly composed of an incident and a reflected wave, so that it is spatially sparse and can be represented with a few elementary waves. For such a sparse problem, the use of compressive sensing (CS)¹⁹ is well-suited, and improves the quality of the reconstruction.^{20,21}

Like other methods in the literature,^{6–11} the proposed methodology can estimate the angle dependence of the surface impedance, which cannot be measured with the standardized methods.^{1,2} The particularity of the present technique is that it is based on the reconstruction of the actual sound field (pressure and particle velocity) on the surface of the sample. Although this study focuses on free-field measurements, the method can be used to measure the surface impedance of materials *in situ*, in more complex acoustic environments. The design of the method is based on a simplified representation of the sound field, in free-field conditions, assuming specular reflection on the material, and disregarding the influence of the sample's finiteness. Still, these effects occur in a measured sound field and have an impact on the results.

This paper is organized as follows: the theoretical aspects and the methodology are first presented in Sec. II, then two simulation examples are treated in Sec. III. Section IV presents measurements performed in an anechoic room. Finally, the strengths and limitations of the proposed method are discussed in Sec. V.

^{a)}Electronic mail: apar@elektro.dtu.dk

II. THEORY

A spherical coordinate system $\mathbf{r} = (r, \theta, \varphi)$ is used, where r is the radius, θ the polar angle, and φ the azimuth angle, as defined in Fig. 1. The notation $\Omega = (\theta, \varphi)$ is used for simplification. The time convention is implicit and chosen as $e^{j\omega t}$. The medium (air) is characterized by a constant density ρ and a speed of sound c .

The measurements are performed with a rigid spherical array of radius a , positioned at the origin of the coordinate system ($r=0$). The array contains K flush-mounted microphones. The method makes use of these measurements to reconstruct the sound field on a studied surface. The impedance of this surface is derived from the reconstructed pressure and particle velocity.

A. S-ESM and sparsity framework

The S-ESM¹⁸ and its application to compressive sensing^{20,21} are summarized. The pressure is measured at K known microphone positions on the rigid spherical array and is expressed as the sum of L elementary waves, using a set of orthogonal functions $Y_n^m(\Omega)$, i.e., spherical harmonics.¹⁴ The elementary waves are spherical waves originating from L equivalent point sources, situated at $(r_{0,l}, \Omega_{0,l})$, $l=1, \dots, L$. In the general case, the method is used to model a homogeneous and source-free volume (all acoustic sources are outside of it). It is thus common practice to place the equivalent sources outside the volume (to avoid their singularity), and distribute them uniformly, so that it is possible to model waves traveling in any direction.¹⁸ The choice of equivalent source positions used in this study is explained further in Sec. II B. The measured pressure at a position (a, Ω) on the sphere takes the expression¹⁸

$$p_t(a, \Omega) = - \sum_{l=1}^L \frac{j\rho c Q_l}{a^2} \sum_{n=0}^{\infty} \sum_{m=-n}^n \frac{h_n^{(2)}(kr_{0,l})}{h_n^{(2)}(ka)} \times Y_n^m(\Omega) Y_n^{m*}(\Omega_{0,l}), \quad (1)$$

where Q_l is the volume velocity of the l th point source, k is the wave number, and $h_n^{(2)}$ is the spherical Hankel function of the second kind. This expression includes the scattering by the rigid sphere. When Eq. (1) is computed, it is necessary to truncate the infinite sum to an order N , which should satisfy the condition $(N+1)^2 \geq K$ for uniformly distributed microphones.^{16,22} Equation (1) shows that p_t is a linear combination of a set of unknown volume velocities Q_l .

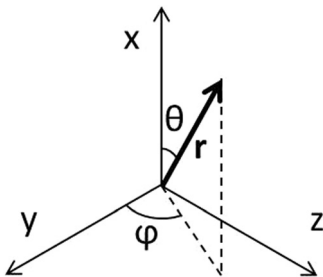


FIG. 1. Spherical coordinate system.

Therefore, the vector of measured complex pressures \mathbf{p}_t at the K microphone positions can be expressed in a matrix form,

$$\mathbf{p}_t = \mathbf{H}\mathbf{q}, \quad (2)$$

where \mathbf{q} is the vector of the unknown volume velocities of the equivalent sources. The number of equivalent sources is usually much larger than the number of measured points, making Eq. (2) an underdetermined system, which requires regularization.

Solving Eq. (2) for \mathbf{q} leads to an estimate of the volume velocities of the equivalent sources $\tilde{\mathbf{q}}$, which can be used to reconstruct the sound pressure at M arbitrary points with¹⁸

$$\tilde{\mathbf{p}}_r = \mathbf{G}\tilde{\mathbf{q}}, \quad (3)$$

where \mathbf{G} is a free-field transfer matrix of size $M \times L$. Note that the scattering by the rigid sphere does not appear in the reconstructed field as it is not included in the matrix \mathbf{G} . It is also possible to reconstruct the particle velocity from $\tilde{\mathbf{q}}$ by applying Euler's equation to Eq. (3).¹⁸

Assuming that the chosen equivalent sources cover all directions of arrival, a spatially sparse sound field composed of waves from a few directions is represented by a sparse vector \mathbf{q} with a few non-zero coefficients. In that case, the sparsity of the solution of Eq. (2) can be favored with ℓ_1 -minimization,^{19,20,23} by solving

$$\tilde{\mathbf{q}} = \underset{\mathbf{q}}{\operatorname{argmin}} \|\mathbf{q}\|_1 \quad \text{subject to } \|\mathbf{H}\mathbf{q} - \mathbf{p}_t\|_2 \leq \varepsilon, \quad (4)$$

where ε is an estimate of the noise floor of the measurement. This equation is valid if the solution is sparse and the matrix \mathbf{H} has incoherent columns.¹⁹ This approach is referred to as CS. Equation (4) is a convex optimization problem that we solve with a package called CVX.²⁴ The optimization problem can also be expressed in an unconstrained form, known as LASSO.²⁵

If spherical spreading can be neglected, it is possible to expand the sound field as a sum of L plane waves originating from the directions $\Omega_{0,l}$. In that case, Eq. (1) is replaced by²⁶

$$p_t(a, \Omega) = - \sum_{l=1}^L \frac{4\pi p_{0,l}}{(ka)^2} \sum_{n=0}^{\infty} \sum_{m=-n}^n \frac{j^{n+1}}{h_n^{(2)}(ka)} Y_n^m(\Omega) Y_n^{m*}(\Omega_{0,l}), \quad (5)$$

where $p_{0,l}$ is the amplitude of the l th plane wave. Note that if a point source expansion is used, as in Eq. (1), the solution vector consists of the volume velocities Q_l , whereas when a plane wave expansion is used, Eq. (5), the solution vector consists of the amplitudes $p_{0,l}$.

B. Single reflection in free-field

The wave expansion method presented in Sec. II A is used to estimate the surface impedance of a large horizontal sample. The sound field originates from a single wave at oblique incidence, which is reflected on the studied sample. The spherical array is placed close to the surface of the sample,

with the distance between the array's center and the surface denoted as d . The sample is approximated as an infinite plate so that diffraction from the edges is ignored. This approximation is commonly made in most previous methods.^{6–11} We expect the sound field to be spatially sparse, consisting mainly of an incident wave and a reflected wave. For instance, it is common to model the reflection of a point source with a virtual image source, which is symmetrical to the primary source with respect to the sample, as seen in Fig. 2.

We consider either Eq. (1) or Eq. (5) as a wave expansion, depending on the nature of the sound field. Although the plane wave formulation is simpler, equivalent point sources make it possible to account for spherical spreading and to describe the near-field term of the particle velocity, which is physically more correct if the sound source is close to the sample. The chosen elementary waves have uniformly distributed directions of arrival to ensure that a spatially sparse sound field can be represented with a sparse vector. In more complex environments, it also makes it possible to localize and eliminate unwanted noise, such as scattered waves or secondary reflections. In addition, for the point source expansion, the equivalent sources are placed on a sphere centered on the sample, so it contains the position of the source and the image source, as shown in Fig. 2. When measuring an actual sound field, the equivalent sources are expected to represent fairly well the reflection, especially in terms of position of the source and the image source. However, additional effects can appear, such as edge diffraction or scattering on the surface.

The sound field is reconstructed on the sample,¹⁸ as shown in Fig. 2. In the examples given in Secs. III and IV, the pressure and the normal component of the particle velocity are calculated on $M=21 \times 21$ points positioned on a square grid of $10 \times 10 \text{ cm}^2$ centered on the z axis. The position of the grid is chosen to minimize the backpropagation distance in order to improve the accuracy of the reconstruction. The normalized surface impedance on the material can be calculated with

$$Z_S(\mathbf{r}_i) = -\frac{1}{\rho c u_z(\mathbf{r}_i)} \frac{p(\mathbf{r}_i)}{u_z(\mathbf{r}_i)}, \quad i = 1, \dots, M. \quad (6)$$

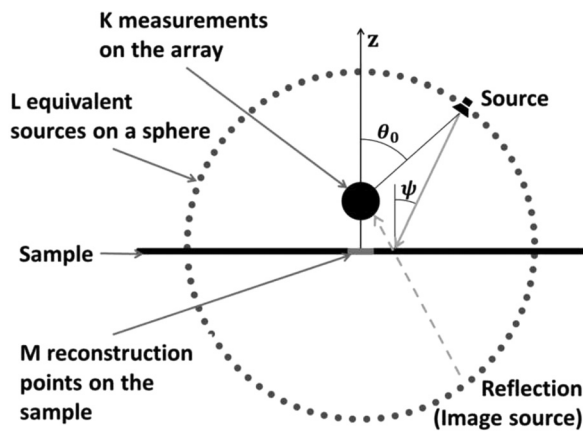


FIG. 2. Measurement principle to determine the surface impedance of a given sample using S-ESM.

Note that the surface impedance is generally a differential operator due to wave propagation and surface effects,²⁷ so Eq. (6) is an approximation. The material's estimated surface impedance \tilde{Z}_S is taken as the spatial average of all the results from Eq. (6) over the grid,

$$\tilde{Z}_S = \langle Z_S(\mathbf{r}_i) \rangle_{i=1, \dots, M}. \quad (7)$$

The spatial averaging $\langle \cdot \rangle$ is done in order to eliminate the effect of random errors, and to obtain a single number for Z_S . The grid is small enough to ensure not too large spatial variations of Z_S in the frequency range of interest. Finally, the estimated absorption coefficient is obtained using²⁸

$$\tilde{\alpha} = 1 - \left| \frac{\tilde{Z}_S \cos(\psi) - 1}{\tilde{Z}_S \cos(\psi) + 1} \right|^2, \quad (8)$$

where ψ is the angle of incidence. This equation was established in the case of plane wave incidence on an infinite sample,²⁹ but it is used here as an approximation, even for spherical wave incidence and finite samples.

Previous studies^{16,18} show that the scattering of the reflected field by the array is negligible, even when the surface is fully reflective.¹⁸

III. NUMERICAL RESULTS

The simulated sample is an infinite plate of porous material. Miki's model³⁰ is used to calculate the sample's characteristic impedance Z_c and propagation constant γ from its flow resistivity σ and its thickness h . Under a plane wave assumption and with a rigid backing, the surface impedance is obtained as³¹

$$Z_S = -jZ_c \frac{k}{k_n} \cot(k_n h), \quad (9)$$

where $k_n = \sqrt{-\gamma^2 - k^2 \sin^2(\psi)}$. Note that Z_S varies with the incidence angle ψ , which shows that this is not a locally reacting model. In this section, we use $h=10 \text{ cm}$ and $\sigma=12\,900 \text{ Nsm}^{-4}$, which correspond to the tested sample in Sec. IV.

The method is tested for an incident plane wave (Sec. III A) and an incident spherical wave (Sec. III B). Gaussian noise is added to the simulated pressure with a signal-to-noise ratio (SNR) of 30 dB. The array has a radius $a=9.75 \text{ cm}$ and 64 uniformly distributed microphones. For such an array, the minimum truncation order is $N=7$. The distance between the array's center and the sample is $d=19.75 \text{ cm}$ (10 cm distance between the array's surface and the material). The studied frequencies are the center frequencies of 1/24 octave bands spanning from 100 to 4000 Hz, which concurs with the array's working range.¹⁶ 256 elementary waves with uniformly distributed directions are used, as a compromise between spatial resolution and computation speed. The noise floor ε in Eq. (4) is calculated for each frequency as

$$\varepsilon = \|\mathbf{p}_t\|_2 \cdot 10^{-(L_{\text{SNR}}/20)}. \quad (10)$$

A. Case 1: Plane wave incidence

First, the method is tested for incident plane waves, at incidence angles of 0° , 30° , and 60° .

For an incident plane wave of amplitude p_0 , the reflected field is also a plane wave of amplitude p_1 with a symmetrical direction of arrival with respect to the sample's surface. The amplitude of the reflected wave is characterized by a plane wave reflection coefficient defined by

$$R = \frac{p_1}{p_0} = \frac{Z_S \cos(\psi) - 1}{Z_S \cos(\psi) + 1}. \quad (11)$$

In this particular example, the incoming sound field on the array is only composed of plane waves. Thus, a plane wave model, following Eq. (5), is used in this section, instead of a point source model, as in the rest of the paper.

Examples of estimated coefficients at 125 and 500 Hz are shown in Fig. 3. The magnitude of the coefficients is represented in dB. The scale covers 30 dB, and its maximum corresponds to the incident pressure amplitude. In general, a sparse solution is obtained where both the directions of the incident and reflected waves are clearly identified, as illustrated at 500 Hz. However, the estimation becomes less

accurate at low frequencies and large incidence angles. At 125 Hz, the localization is still effective at 0° and 30° , but it loses accuracy at 60° . This is due to the wavelength being much larger than the array's dimensions, making the recorded information redundant across the microphones. In addition, at higher angles of incidence, the angular distance between the incident and the reflected wave is reduced, making it more difficult to separate these two components.

The sound field is reconstructed on the sample ($z = -d$), at 21×21 points on a square grid of dimensions $10 \times 10 \text{ cm}^2$ centered on the z axis. The quality of the reconstruction is assessed with the relative reconstruction error, defined for pressure as

$$\epsilon_p = \frac{\|\tilde{\mathbf{p}} - \mathbf{p}_{\text{true}}\|_2}{\|\mathbf{p}_{\text{true}}\|_2}, \quad (12)$$

where $\tilde{\mathbf{p}}$ is the vector of the reconstructed pressures at each point of the grid and \mathbf{p}_{true} is the vector of the true pressures at the same points. This error is also expressed in a dB scale using

$$L_{\epsilon,p} = 20 \log_{10}(1 + \epsilon_p). \quad (13)$$

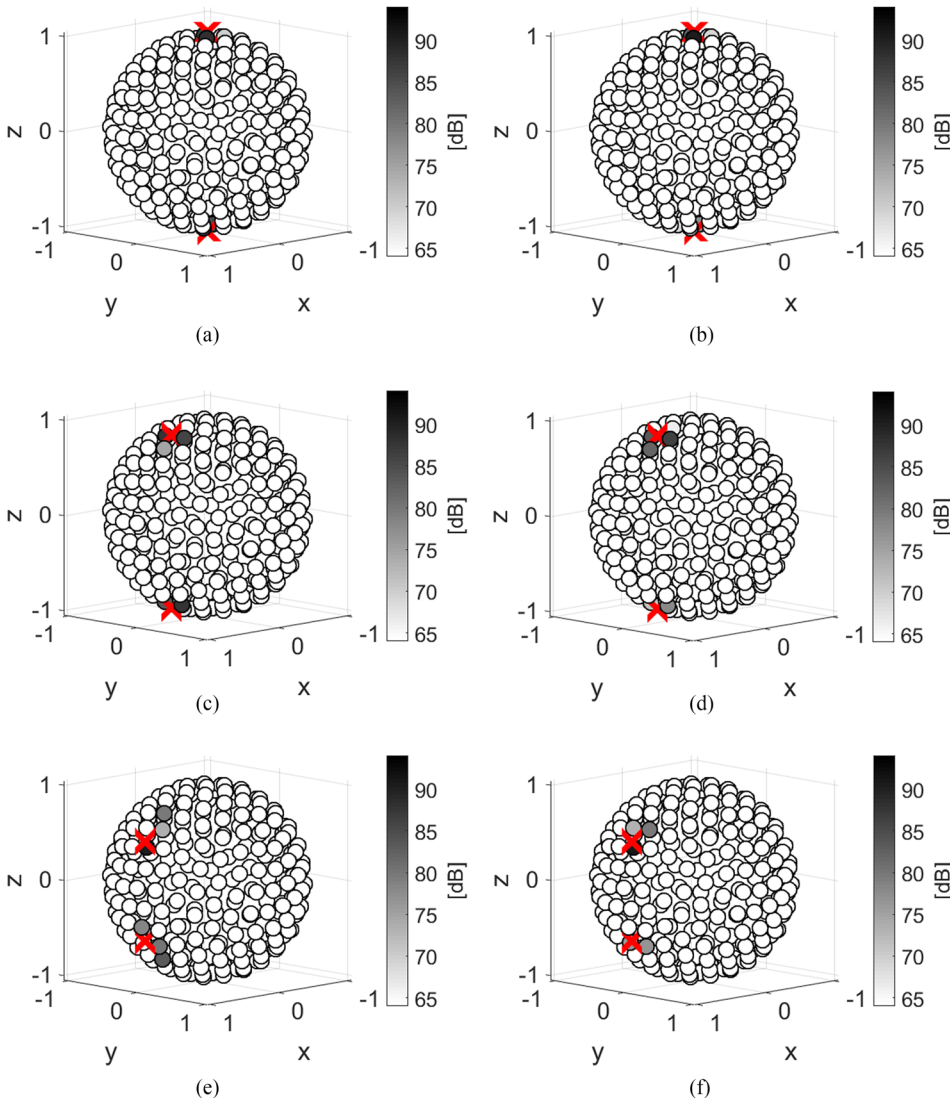


FIG. 3. (Color online) Magnitude of the estimated coefficients in dB re. $20 \mu\text{Pa}$ at 125 and at 500 Hz for the simulation of an incident plane wave. The crosses indicate the directions of the incident wave and the reflected wave. (a) 125 Hz, 0° ; (b) 500 Hz, 0° ; (c) 125 Hz, 30° ; (d) 500 Hz, 30° ; (e) 125 Hz, 60° ; (f) 500 Hz, 60° .

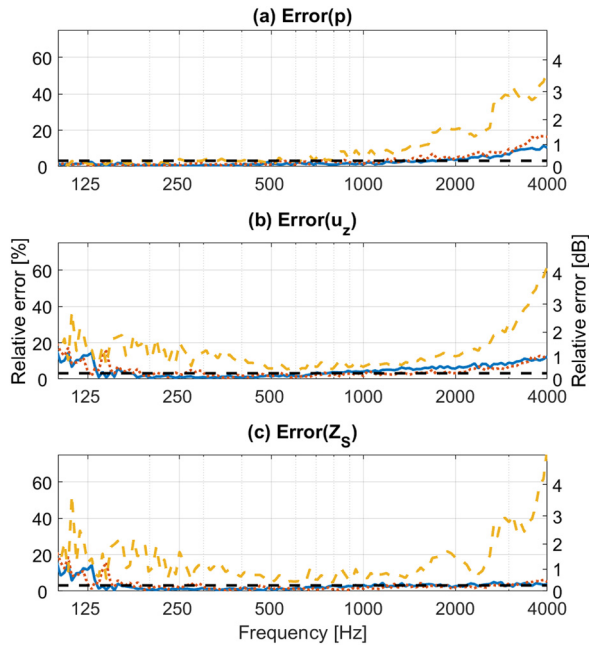


FIG. 4. (Color online) Relative reconstruction error on pressure (a), normal component of particle velocity (b), and surface impedance (c) for plane wave incidence in the presence of noise (SNR 30 dB). Angles of incidence 0° (—), 30° (···), and 60° (---).

Analogous expressions are used for the particle velocity and the impedance errors.

Figure 4 shows the relative pressure, velocity, and impedance errors as a function of frequency, in percentage and in decibels. The black dashed line corresponds to the noise floor, given by $10^{-(L_{\text{SNR}}/20)} = 3.2\%$. At 0° and 30°, the pressure error is lower than the noise floor for frequencies below

2000 Hz, and the velocity error for frequencies between 150 and 1000 Hz. Both the pressure and velocity errors increase at higher frequencies for the three incidence angles, due to the backpropagation distance becoming larger than the wavelength. At low frequencies, the pressure is accurately estimated, as Eq. (4) minimizes the error in pressure on the array, and the reconstruction distance is much smaller than the wavelength. Conversely, the poorer estimation of the plane wave coefficients observed in Fig. 3 affects the reconstruction of the particle velocity, especially at 60°. Indeed, the particle velocity is a relatively small quantity at low frequencies, as dependent on the pressure gradient, which makes it more sensitive to noise.^{18,32} In addition, the quantity of interest is the normal component of the particle velocity, which is mainly reconstructed from the elementary plane waves with normal directions. This becomes problematic at larger angles of incidence, where the sound field is represented by waves with a small normal particle velocity component. In that case, Eq. (6) is close to a singularity, for $u_z \rightarrow 0$. For instance, in Fig. 3(e), the incident and the reflected field are represented by three waves each. The directions closer to the normal predominate in the calculation of u_z , although they do not correspond to actual sound field components. This amplifies the estimation error. Finally, the resulting error in impedance remains below 20% for 0° and 30° incidence with a slight rise at low frequencies, but it is consistently higher at 60°—the impedance error is below 20% only between 250 Hz and 1800 Hz. The impedance error is mainly ascribed to the errors in the particle velocity estimation.

The estimated impedance and absorption coefficient can be seen in Fig. 5. The surface impedance calculated from Miki's model shows very little variation with the incidence

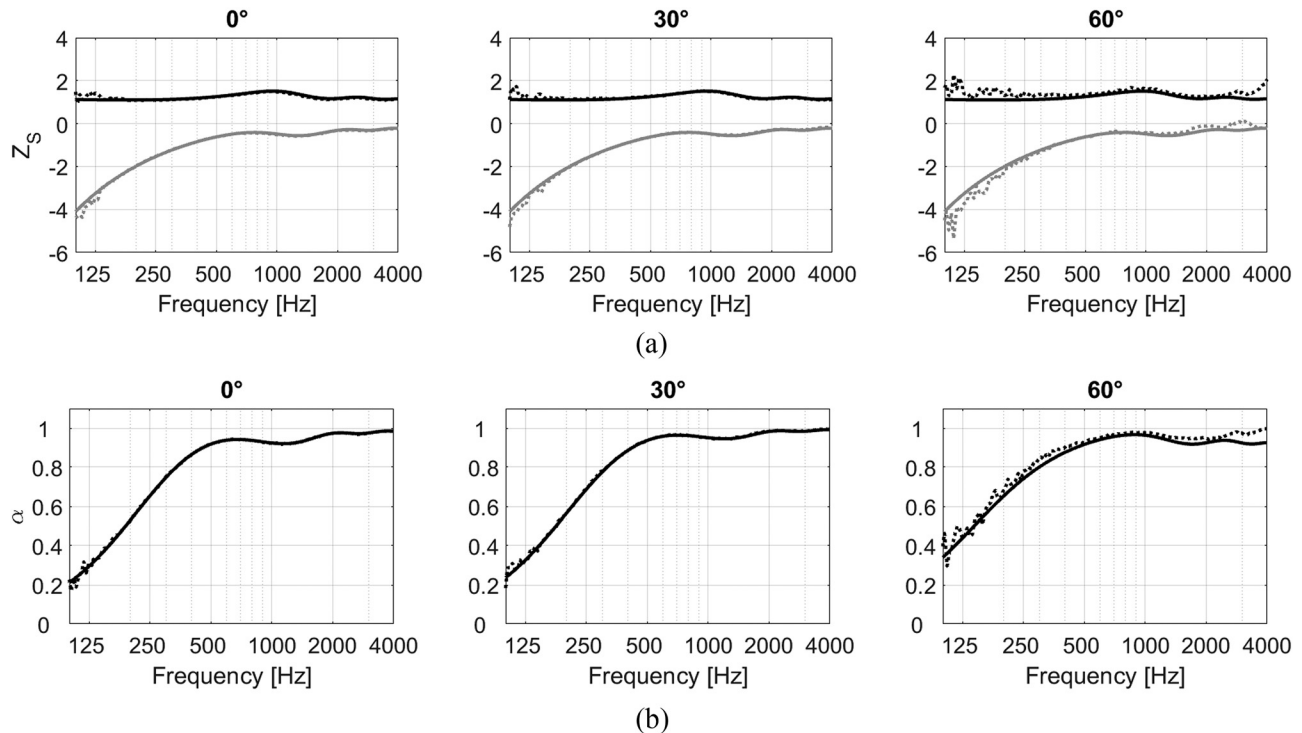


FIG. 5. Surface impedance and absorption coefficient for plane wave incidence, from Miki's model (—) and from the simulation (···). (a) Surface impedance. Real part in black, imaginary part in gray. (b) Absorption coefficient.

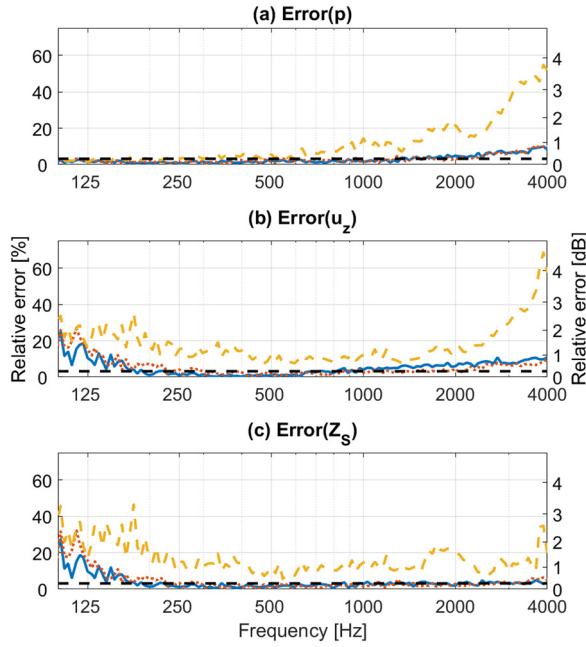


FIG. 6. (Color online) Relative reconstruction error for spherical wave incidence with a SNR of 30 dB. (a) pressure, (b) normal component of particle velocity, and surface impedance (c). Angles of incidence 0° (—), 30° (···), and 60° (---).

angle up to 60° , which indicates that a local reaction approximation could be valid in this simulation. The method succeeds to give accurate estimates of the material's impedance and its absorption coefficient between 200 Hz and 4 kHz. The estimation presents small deviations at high frequencies due to errors in the field reconstruction. The presence of noise affects mostly the low frequencies and the larger

angles of incidence. Furthermore, although more important errors appear at 60° , the estimation still follows the same trend as the reference value.

B. Case 2: Spherical wave incidence

The impedance estimation method is tested with a sound field originating from a point source. The source is placed 1.5 m from the array's center at different polar angles θ_0 (0° , 30° and 60°); the corresponding angles of incidence ψ are 0° , 24° and 48° . Equivalent point sources are used for the sound field reconstruction, following Eq. (1). The simulation of the sound field follows a formulation described by Wenzel³³ and Thomasson.³⁴ The procedure to obtain the sound field scattered by the spherical array is described in the Appendix.

The reconstruction is done on a square grid at $z = -d$, of dimensions $10 \times 10 \text{ cm}^2$, consisting of 21×21 points and centered on the z axis. The relative reconstruction errors of the sound field quantities are calculated using Eq. (12) and plotted in Fig. 6 as a function of frequency. The pressure error increases with frequency, especially at 60° . Indeed, using equivalent point sources increases the ill-posedness of the problem as the pressure decay with distance needs to be accounted for. The particle velocity error also becomes larger at low frequencies. Indeed, the particle velocity is reconstructed as the sum of the particle velocities of equivalent spherical waves, which have a large nearfield term at low frequencies. This tends to amplify errors in the estimation of the source strengths.¹⁸ In any case, the impedance error is similar to the plane wave case (Fig. 4), with an error around the noise floor level at 0 and 30° above 200 Hz. The

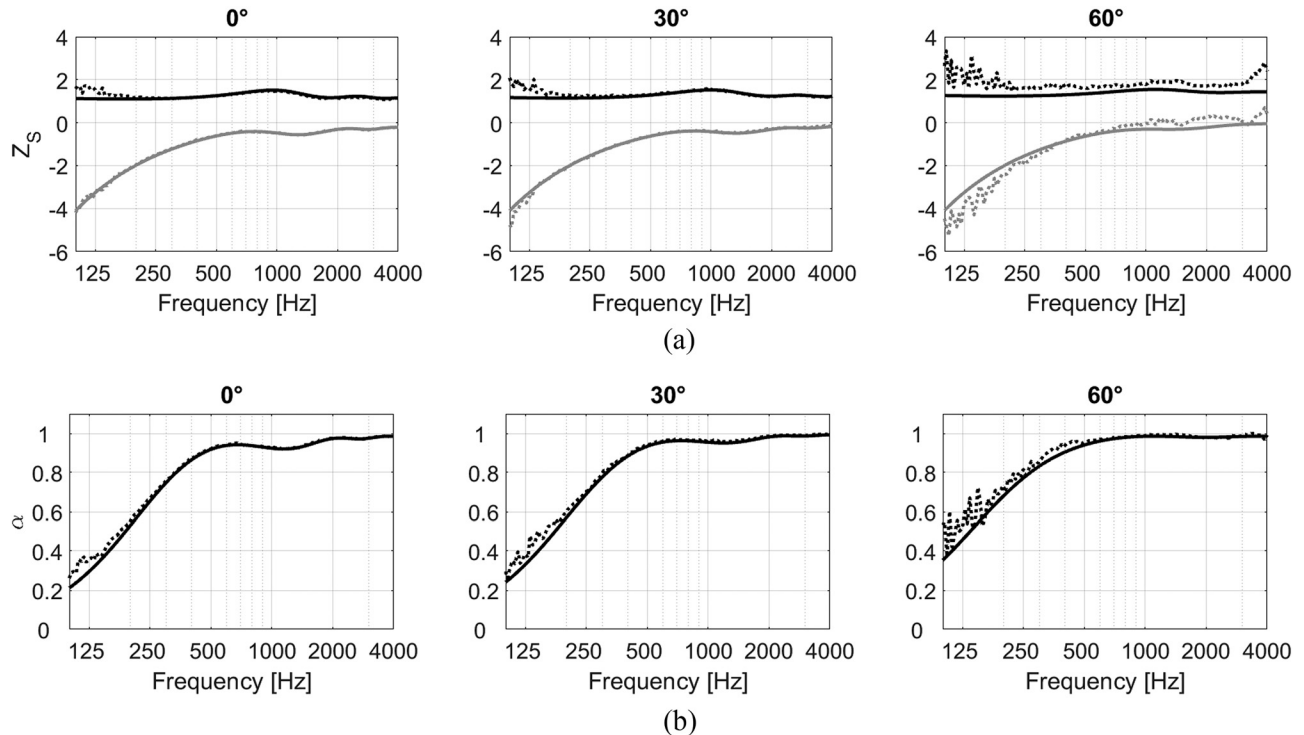


FIG. 7. Surface impedance and absorption coefficient for spherical wave incidence. Miki's model (—), estimation from the simulation (···). (a) Surface impedance. Real part in black, imaginary part in gray. (b) Absorption coefficient.

60° case presents an error greater than 20% outside the range 250–1600 Hz, and a minimum of 6%, which is still above the noise floor.

Figure 7 shows the resulting estimation of both the impedance and the absorption coefficient at the three angles of incidence. The result is accurate and quite robust to noise above 200 Hz, with larger discrepancies appearing for a polar angle of 60°, although the trend is similar.

In summary, these two examples (Secs. III A and III B) demonstrate that the surface impedance of a given material can be properly estimated, with limitations appearing at 60°. The frequency range of validity decreases when the angle of incidence increases. The quality of the estimation depends on the accuracy of the reconstructed pressure and velocity. It was also shown that the particle velocity is more prone to errors, especially at low frequencies, which is in accordance with previous findings.^{18,32,35}

IV. EXPERIMENTAL RESULTS

The proposed method is tested experimentally with a similar setup to the simulation in Sec. III B. The measurements take place in a large anechoic room at the Technical University of Denmark, with an approximate volume of 1000 m³, ensuring free field conditions down to 50 Hz.³⁶ The experimental setup is presented in Fig. 8. The tested sample is a large plate of mineral wool of dimensions 1.8 m × 2.4 m, thickness 10 cm, and flow resistivity 12900 Nsm⁻⁴. This

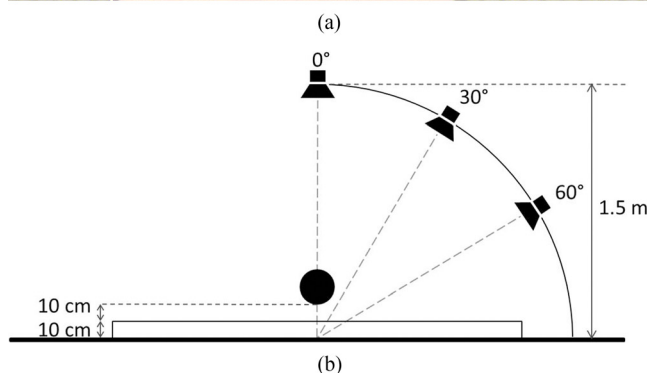


FIG. 8. (Color online) Measurement setup in DTU's large anechoic chamber. The spherical array and the omnidirectional source are hung above the rectangular sample. The three studied positions are shown in the drawing (b).

sample is placed on a rigid backing plate with a surface of about 14 m². The rigid spherical array has a radius of 9.75 cm and 64 prepolarized $\frac{1}{4}$ in. microphones, which are uniformly distributed over the surface. The array's center is positioned above the sample under test at a height $d = 19.75$ cm. The sound source is an OmniSource Loudspeaker type 4295 produced by B&K (Nærum, Denmark) driven with white noise. The source is placed on a half-circle of radius 1.5 m centered on the backing plate. Three source positions are studied, at 0°, 30°, and 60° from the normal, as presented in Fig. 8(b); the corresponding incidence angles ψ are 0°, 28°, and 57°. The data are processed by a B&K PULSE analyzer, where the fast Fourier transform (FFT) of the signal is calculated with a frequency resolution of 1 Hz and a bandwidth of 6400 Hz. A Hanning window is used and at least 200 averages are taken with 75% overlap. The sound field reconstruction is carried out using a point source expansion as in Eq. (1). As in Sec. III, the reconstruction points are distributed on a square grid of dimensions 10 × 10 cm² with 21 × 21 points on the specimen.

The determination of the parameter ε in Eq. (4) is crucial to estimate \mathbf{q} in Eq. (2), as it serves as a stopping criterion in the optimization algorithm. If ε is greater than the actual noise floor in the measurement, there is a risk of discarding the reflected wave as noise. If it is lower than the actual noise floor, then the solution is contaminated by noise and may present additional components. However, in the experimental setup, other sources of error add up to the presence of background noise, such as positioning errors or mismatch between the transducers. As a result, the single transducer SNR may not correspond to the true noise floor as in Eq. (10). In addition, the measured SNR is mostly around 45 dB but with important frequency variations, which indicates that ε is also frequency dependent. In this study, a choice of ε corresponding to a SNR of 28 dB—mostly above the actual noise floor—yields a spatially sparse wave configuration, with visible incident and reflected directions only. The optimal choice of ε has been addressed in the literature^{23,37} and is out of the scope of this paper.

Examples of equivalent source coefficients at 500 Hz and 1000 Hz are shown in Fig. 9. At 500 Hz, for the three source positions, the non-zero components of $\tilde{\mathbf{q}}$ are found close to the source and image source locations. At 60°, the representation of the reflected field does not match with the image source, which may indicate that reflection approaching grazing incidence is no longer specular. At 1000 Hz, deviations appear at 30° and 60°. Especially at 60°, the reflected field is not detected, probably due to a too high absorption. However, it is difficult to determine if the observed deviations are due to actual physical phenomena or to a faulty source strength estimation.

The measured surface impedance and absorption coefficient are presented in Fig. 10. A simulation with an infinite sample is also plotted, where the sample's surface impedance is derived from Miki's model. The estimates from the simulation are the average of 10 runs with different noise realizations. We use the surface impedance and the absorption coefficient derived from Miki's model for reference. At 0°, we also include the absorption coefficient measured in an

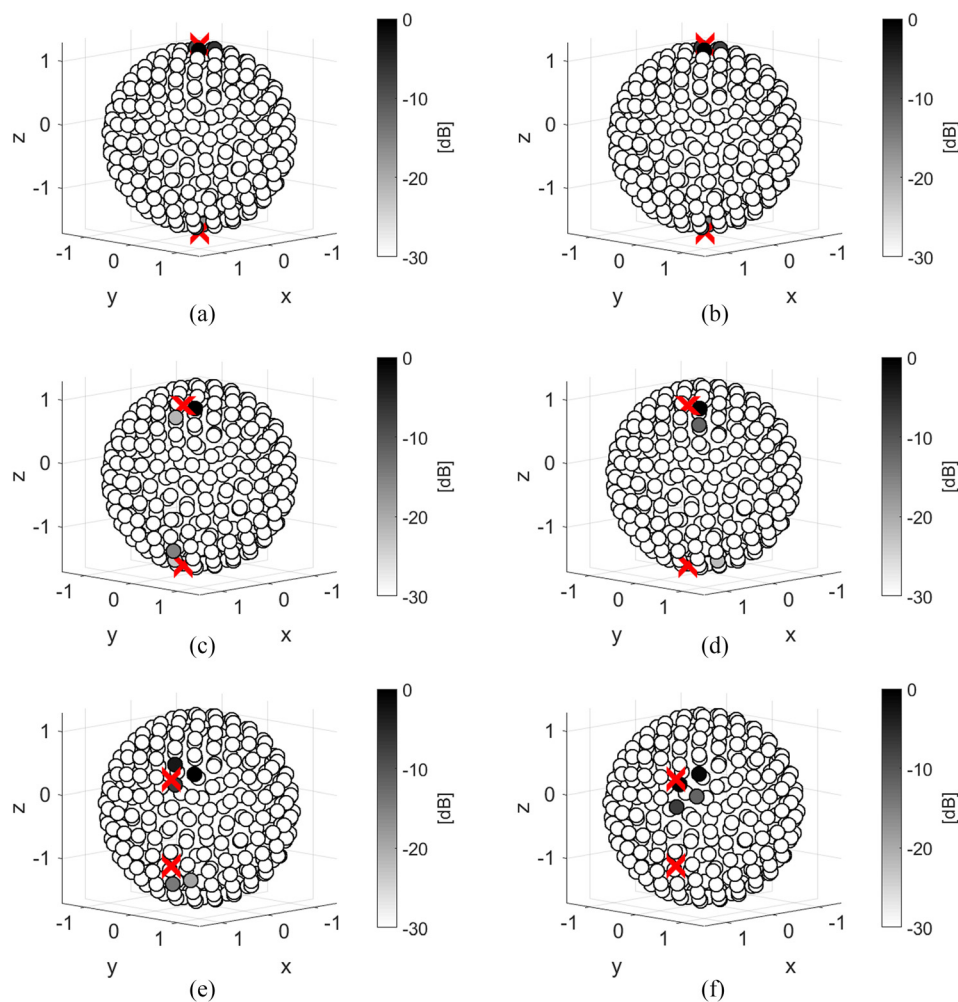


FIG. 9. (Color online) Magnitude of the estimated equivalent source coefficients at 500 Hz and 1000 Hz from experimental measurements, in dB relative to the maximum. The crosses indicate the positions of the source and the image source. (a) 500 Hz, 0° ; (b) 1000 Hz, 0° ; (c) 500 Hz, 30° ; (d) 1000 Hz, 30° ; (e) 500 Hz, 60° ; (f) 1000 Hz, 60° .

impedance tube as additional reference. First, in Fig. 10(b) at 0° , the impedance tube measurement and Miki's model differ. Above 300 Hz, the microphone array measurement is actually closer to the impedance tube result than to Miki's model. This indicates that Miki's model is not an ideal reference. It is an empirical model, which relies on assumptions including the isotropy of the material. It also depends on the quality of the flow resistivity measurement. In both Figs. 10(a) and 10(b) at 0° , the simulation follows Miki's model, except at low frequencies, due to the reconstruction errors discussed in Sec. III B. The measured surface impedance and absorption coefficient follow globally the same trend as the simulation. In addition, we observe oscillations below 300 Hz in the experimental curves, due to diffraction from the edges of the sample. The obtained absorption curves are similar to other studies made on finite samples, which also showed oscillations at low frequencies.³⁸ At 30° , Figs. 10(a) and 10(b) show again a good agreement between the simulation and Miki's model, with errors appearing below 250 Hz. As in the normal incidence case, the measurement results generally follow the simulation and present oscillations below 250 Hz. The 60° case illustrates the limits of the method. As discussed in Sec. III B, more important reconstruction errors limit the accuracy of the estimated impedance. In Fig. 10(a), the simulated result at 60° is much less accurate than for smaller angles of incidence, especially

below 250 and above 3000 Hz. The measured surface impedance shows a larger deviation and even more pronounced oscillations. These oscillations are attributed to edge diffraction at low frequencies. Additionally, on the whole frequency range, the normal component of the particle velocity is smaller towards grazing incidence, and therefore more sensitive to noise.

In summary, a good agreement is found between the measured impedance and the available references for the angles 0° and 30° and for frequencies above 300 Hz. At lower frequencies and larger angles of incidence, edge diffraction effects, which were not accounted for, dominate and disrupt the results.

V. DISCUSSION

The numerical and experimental results prove the validity of the presented method for angles below 60° and between 200 and 4000 Hz. It is possible to estimate an angle-dependent surface impedance, which cannot be obtained with neither of the two standardized methods. Moreover, the different sound field components can be easily determined, in terms of their amplitudes and directions of arrival, as shown in Figs. 3 and 9. This makes it possible to detect, in principle, other sound field components such as reflections, diffraction from edges and extraneous sources.

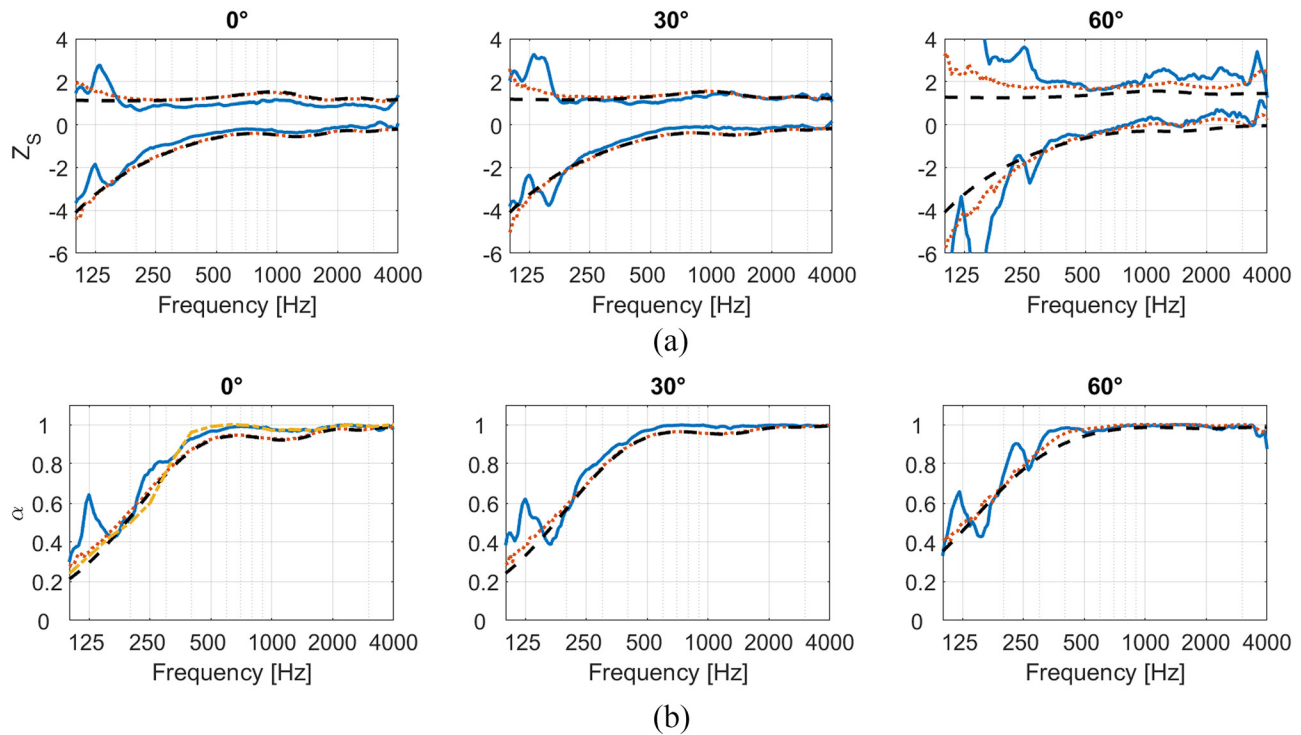


FIG. 10. (Color online) Estimated surface impedance and absorption coefficient from experimental measurements (—) and from simulations (···) at 0°, 30°, and 60° incidence. Comparison with Miki's model (---) and an impedance tube measurement (- · -). (a) Surface impedance. The real part is positive and the imaginary part negative. (b) Absorption coefficient.

Another particularity of the method is that the impedance is inferred directly from the reconstructed sound field on the material's surface, whereas methods such as in Refs. 8–11 rely on the estimation of the reflection coefficient. Finally, it should be noted that not much prior information on the setup is used in the processing, apart from assuming spatial sparsity (i.e., few waves). The method could be improved by including such information; for instance the knowledge of the source positions,^{16,39} or ensuring that the incident power is larger or equal to the reflected one. The method can be used *in situ*, where the measurement takes place in an ordinary room. It should be noted that in this case, the sound field is fundamentally different, due to the presence of secondary reflections, and especially due to the modal behavior of the sound field at low frequencies.

Limitations in terms of frequency and incidence angle were identified. At high frequencies, the backpropagation distance limits the accuracy of the result. Reducing this distance, for instance using transducers close to the surface of the sample, would be beneficial. The largest errors occur when the trace wavelength in the normal direction is much larger than the array, namely at low frequencies and at grazing incidence, where the amplitude of the normal particle velocity is smaller. Indeed, the impedance estimation is particularly affected by errors in the normal particle velocity estimation. It can be noted that a more robust reconstruction of particle velocity is possible using velocity sensors.⁴⁰

In addition, a better knowledge of the sound field could improve the method. In particular, the finiteness of the sample has a considerable impact on the experimental results at low frequencies, as shown in Fig. 10. If one wants to

characterize the material independently of its size and shape, the influence of edge diffraction should be identified and compensated for. For instance, it is possible to formulate the effect of finiteness as a radiation impedance²⁹ and include it in the absorption calculation.⁴¹ This approach does not rely on the estimation of the normal particle velocity, which might be beneficial. Nevertheless, it relies on the quality of the model used to characterize edge diffraction, which also makes it more case dependent. Furthermore, the sphericity of the wave front should be included in the calculation of Z_s and α .

Finally, the actual impedance and absorption coefficient values are only partially known, which complicates the validation of the experimental results. At normal incidence, the impedance tube method can be used as a reference, but at other incidence angles Miki's model, which is empirical, was used due to the lack of experimental reference data. Miki's model assumes an isotropic material, but it is not the case of the tested sample, which is fibrous.

VI. CONCLUSION

This paper shows how microphone array measurements can be used to estimate a sample's surface impedance by sound field reconstruction. In particular, the use of S-ESM¹⁸ and CS lead to an accurate sound field reconstruction,^{20,23} which enhances the quality of the impedance estimation, especially at mid and high frequencies.

The simulations presented in this study show the validity of the method between 200 and 4000 Hz (the operating frequency range of the array). Discrepancies appearing at 60° incidence also illustrate the difficulty to estimate the

surface impedance approaching grazing incidence, due to the trace wavelength being much larger than the array and the normal component of the particle velocity being smaller.

Experimental results in laboratory conditions show a good agreement with reference data above 300 Hz and for angles below 60°. Challenges still to be addressed are the finiteness of the studied samples, the estimation close to grazing incidence, and the characterization of the measurement noise.

ACKNOWLEDGMENTS

The authors would like to thank Mélanie Nolan for the discussions, comments on the manuscript, and for the impedance tube measurement data. The measurements were performed as part of a project funded by the Danish Sound Innovation Network, entitled *In situ acoustic impedance estimation based on sparse array processing*, in collaboration with Brüel & Kjær, Bang & Olufsen, Ecophon, and Odeon. The authors would like to acknowledge their contribution to experimental tests.

APPENDIX: CALCULATION OF THE SOUND FIELD ORIGINATING FROM A POINT SOURCE

In the simulation, Sec. III B, a model for the reflection of spherical waves by an infinite plane is needed. A spherical reflection factor formulation⁴² was initially tested, but the resulting pressure proved to be inaccurate at low frequencies and larger angles of incidence. Instead, an expression proposed by Wenzel³³ is used,

$$p = \frac{j\omega\rho Q}{4\pi R_1} e^{-jkR_1} + \frac{j\omega\rho Q}{4\pi R_2} e^{-jkR_2} + p_R. \quad (\text{A1})$$

The two first terms correspond to an equal contribution from a point source and an image source. The term p_R is a correction term, which is calculated as

$$p_R = \frac{\rho c k^2 \nu}{2\pi} \int_0^\infty \frac{\kappa e^{-mh}}{m(jk\nu - m)} J_0(\kappa r) d\kappa, \quad (\text{A2})$$

with

$$m = (\kappa^2 - k^2)^{1/2}, \quad \text{Re}(m) \geq 0, \quad (\text{A3})$$

$$h = z + z_0, \quad (\text{A4})$$

$$r = \left[(x - x_0)^2 + (y - y_0)^2 \right]^{1/2}, \quad (\text{A5})$$

(x, y, z) being the coordinates of the receiver point and (x_0, y_0, z_0) the ones of the source. Thomasson proposed an efficient way of computing this integral using a steepest-descent contour.³⁴ The formulation proposed by Thomasson is a series of equations [Eqs. (32) to (41) in Ref. 34], one of them including a semi-infinite integral from 0 to infinity. This term is evaluated numerically using the MATLAB function *integral*, which is a global adaptive quadrature algorithm, with an absolute tolerance of 10^{-10} and a relative tolerance of 10^{-6} .

The scattering by the spherical array is expressed by expanding the incident field in spherical harmonics, but the spherical harmonic expansion of Eq. (A1) is not trivial. Therefore, a plane wave approximation of the incident field is used. This field is assumed to be composed of 1000 uniformly distributed plane waves of unknown amplitudes and is computed at 1000 points on the sphere using Eq. (A1) and Eq. (A2). This leads to the system

$$\mathbf{p}_{\text{inc}} = \mathbf{H}_{\text{PW}} \mathbf{A}_{\text{PW}}, \quad (\text{A6})$$

where \mathbf{p}_{inc} is the vector of the calculated incident pressures on the sphere, \mathbf{A}_{PW} the unknown plane wave amplitudes and \mathbf{H}_{PW} a transfer matrix of size 1000×1000 . \mathbf{A}_{PW} is estimated by using the pseudo-inverse of \mathbf{H}_{PW} , due to the high condition number of the matrix. The high spatial density of the calculated pressures on the sphere ensures that the sound field is well represented on the spherical array.

Once the plane wave amplitudes \mathbf{A}_{PW} are determined, the scattered pressure at the microphone positions on the sphere can be derived as a superposition of scattered plane waves,

$$\mathbf{p}_t = \mathbf{H}_2 \mathbf{A}_{\text{PW}}. \quad (\text{A7})$$

This equation follows exactly the same idea as Eq. (2), where \mathbf{H}_2 is a transfer matrix between the 1000 plane waves and the K measurement points and includes the scattering by the sphere.

¹ISO 10534-2:1998, “Acoustics—Determination of sound absorption coefficient and impedance in impedance tubes—Part 2: Transfer-function method” (International Organization for Standardization, Geneva, 1998).

²ISO 354:2003, “Acoustics—Measurement of sound absorption in a reverberation room” (International Organization for Standardization, Geneva, 2003).

³G. Marbjerg, J. Brunskog, C.-H. Jeong, and E. Nilsson, “Development and validation of a combined phased acoustical radiosity and image source model for predicting sound fields in rooms,” *J. Acoust. Soc. Am.* **138**, 1457–1468 (2015).

⁴C.-H. Jeong and J. Brunskog, “The equivalent incidence angle for porous absorbers backed by a hard surface,” *J. Acoust. Soc. Am.* **134**, 4590–4598 (2013).

⁵E. Brandão, A. Lenzi, and S. Paul, “A review of the *in situ* impedance and sound absorption measurement techniques,” *Acta Acust. Acust.* **101**, 443–463 (2015).

⁶J. F. Allard and B. Sieben, “Measurements of acoustic impedance in a free field with two microphones and a spectrum analyzer,” *J. Acoust. Soc. Am.* **77**, 1617–1618 (1985).

⁷H. de Bree, R. Lanoye, S. de Cock, and J. van Heck, “*In situ*, broad band method to determine the normal and oblique reflection coefficient of acoustic materials,” in *Proceedings of the Noise and Vibration Conference and Exhibition 2005*, Traverse City, MI (2005).

⁸E. Mommertz, “Angle-dependent *in situ* measurements of reflection coefficients using a subtraction technique,” *Appl. Acoust.* **46**, 251–263 (1995).

⁹M. Tamura, “Spatial Fourier transform method of measuring reflection coefficients at oblique incidence. I. Theory and numerical examples,” *J. Acoust. Soc. Am.* **88**, 2259–2264 (1990).

¹⁰J. Ducourneau, V. Planeau, J. Chatillon, and A. Nejade, “Measurement of sound absorption coefficients of flat surfaces in a workshop,” *Appl. Acoust.* **70**, 710–721 (2009).

¹¹J. Rathsam and B. Rafaely, “Analysis of *in situ* acoustic absorption using a spherical microphone array,” *Appl. Acoust.* **89**, 273–280 (2015).

¹²J. Hald, “Basic theory and properties of statistically optimized near-field acoustical holography,” *J. Acoust. Soc. Am.* **125**, 2105–2120 (2009).

¹³M. R. Bai, J.-G. Ih, and J. Benesty, *Acoustic Array Systems* (Wiley, Singapore, 2013), pp. 151–208.

- ¹⁴E. G. Williams, *Fourier Acoustics: Sound Radiation and Nearfield Acoustical Holography* (Academic, San Diego, 1999), Chaps. 6 and 7.
- ¹⁵E. G. Williams and K. Takashima, "Vector intensity reconstructions in a volume surrounding a rigid spherical microphone array," *J. Acoust. Soc. Am.* **127**, 773–783 (2010).
- ¹⁶F. Jacobsen, G. Moreno-Pescador, E. Fernandez-Grande, and J. Hald, "Near field acoustic holography with microphones on a rigid sphere (L)," *J. Acoust. Soc. Am.* **129**, 3461–3464 (2011).
- ¹⁷A. Granados, F. Jacobsen, and E. Fernandez-Grande, "Regularised reconstruction of sound fields with a spherical microphone array," *Proc. Mtgs. Acoust.* **19**, 055010 (2013).
- ¹⁸E. Fernandez-Grande, "Sound field reconstruction using a spherical microphone array," *J. Acoust. Soc. Am.* **139**, 1168–1178 (2016).
- ¹⁹E. Candes and M. Wakin, "An introduction to compressive sampling," *IEEE Signal Process. Mag.* (2008), pp. 21–30.
- ²⁰E. Fernandez-Grande and A. Xenaki, "Compressive sensing with a spherical microphone array," *J. Acoust. Soc. Am.* **139**, EL45–EL49 (2016).
- ²¹E. Fernandez-Grande, A. Xenaki, and P. Gerstoft, "A sparse equivalent source method for near-field acoustic holography," *J. Acoust. Soc. Am.* **141**, 532–542 (2017).
- ²²B. Rafaely, "Analysis and design of spherical microphone arrays," *IEEE Speech Audio Process.* **13**, 135–143 (2005).
- ²³A. Xenaki, P. Gerstoft, and K. Mosegaard, "Compressive beamforming," *J. Acoust. Soc. Am.* **136**, 260–271 (2014).
- ²⁴M. Grant and S. Boyd, "CVX: Matlab software for disciplined convex programming, version 2.1," <http://cvxr.com/cvx> (2014).
- ²⁵R. Tibshirani, "Regression shrinkage and selection via the lasso," *J. R. Stat. Soc. Ser. B* **58**, 267–288 (1996).
- ²⁶B. Rafaely, "Plane wave decomposition of the sound field on a sphere by spherical convolution," *J. Acoust. Soc. Am.* **116**, 2149–2157 (2004).
- ²⁷J. Brunskog, "The forced sound transmission of finite single leaf walls using a variational technique," *J. Acoust. Soc. Am.* **132**, 1482–1493 (2012).
- ²⁸L. Cremer and H. A. Müller, *Principles and Applications of Room Acoustics, Volume 2* (Applied Science Publishers, London, 1982), p. 109.
- ²⁹S. I. Thomasson, "On the absorption coefficient," *Acta Acust. Acust.* **44**, 265–273 (1980).
- ³⁰Y. Miki, "Acoustical properties of porous materials—Modifications of Delany–Bazley models," *J. Acoust. Soc. Jpn.* **11**, 19–24 (1990).
- ³¹J. F. Allard and N. Atalla, *Propagation of Sound in Porous Media: Modelling Sound Absorbing Materials*, 2nd ed. (Wiley, Chichester, UK, 2009), pp. 29–43.
- ³²F. Jacobsen and Y. Liu, "Near field acoustic holography with particle velocity transducers," *J. Acoust. Soc. Am.* **118**, 3139–3144 (2005).
- ³³A. R. Wenzel, "Propagation of waves along an impedance boundary," *J. Acoust. Soc. Am.* **55**, 956–963 (1974).
- ³⁴S.-I. Thomasson, "Reflection of waves from a point source by an impedance boundary," *J. Acoust. Soc. Am.* **59**, 780–785 (1976).
- ³⁵E. Fernandez-Grande, F. Jacobsen, and Q. Leclère, "Sound field separation with sound pressure and particle velocity measurements," *J. Acoust. Soc. Am.* **132**, 3818–3825 (2012).
- ³⁶F. Ingerslev, P.-K. Müller, and J. Kristensen, "The anechoic chambers at the Technical University of Denmark (Volume 2)," Technical Report, Brüel and Kjær (1968).
- ³⁷P. Gerstoft, A. Xenaki, and C. F. Mecklenbräuker, "Multiple and single snapshot compressive beamforming," *J. Acoust. Soc. Am.* **138**, 2003–2014 (2015).
- ³⁸K. Hirosawa, K. Takashima, H. Nakagawa, M. Kon, A. Yamamoto, and W. Lauriks, "Comparison of three measurement techniques for the normal absorption coefficient of sound absorbing materials in the free field," *J. Acoust. Soc. Am.* **126**, 3020–3027 (2009).
- ³⁹E. Fernandez-Grande and T. Walton, "Reconstruction of sound fields with a spherical microphone array," in *Proceedings of Internoise*, Melbourne (2014).
- ⁴⁰F. Jacobsen and V. Jaud, "Statistically optimized near field acoustic holography using an array of pressure-velocity probes," *J. Acoust. Soc. Am.* **121**, 1550–1558 (2007).
- ⁴¹M. Ottink, J. Brunskog, C.-H. Jeong, E. Fernandez-Grande, P. Trojgaard, and E. Tiana-Roig, "In-situ measurements of the oblique incidence sound absorption coefficient for finite sized absorbers," *J. Acoust. Soc. Am.* **139**, 41–52 (2016).
- ⁴²C. Chien and W. Soroka, "Sound propagation along an impedance plane," *J. Sound Vib.* **43**, 9–20 (1975).